

## 1 Article

# 2 Integrin Mechanosensing relies on Pivot-clip 3 Mechanism to Reinforce Cell Adhesion

4 Andre R. Montes<sup>1</sup>, Anahi Barroso<sup>1</sup>, Wei Wang<sup>2,3</sup>, Grace D. O'Connell<sup>3</sup>, Adrian B. Tepole<sup>\*4</sup>, and Mohammad R.K.

5 Mofrad<sup>\*1,5</sup>

6 <sup>1</sup>Molecular Cell Biomechanics Laboratory, Departments of Bioengineering and Mechanical Engineering, University of  
7 California, Berkeley, California, 94720

8 <sup>2</sup>Berkeley City College, Berkeley, California, 94704

9 <sup>3</sup>Berkeley Biomechanics Laboratory, Department of Mechanical Engineering, University of California, Berkeley, California,  
10 94720

11 <sup>4</sup>Tepole Mechanics and Mechanobiology Laboratory, School of Mechanical Engineering, Purdue University, West Lafayette,  
12 Indiana, 47907

13 <sup>5</sup>Molecular Biophysics and Integrative Bioimaging Division, Lawrence Berkeley National Lab, Berkeley, California, 94720

14 \*Correspondence: mofrad@berkeley.edu, abuganza@purdue.edu

15 ABSTRACT Cells intricately sense mechanical forces from their surroundings, driving biophysical and biochemical  
16 activities. This mechanosensing phenomenon occurs at the cell-matrix interface, where mechanical forces resulting from  
17 cellular motion, such as migration or matrix stretching, are exchanged through surface receptors, primarily integrins, and  
18 their corresponding matrix ligands. A pivotal player in this interaction is the  $\alpha_5\beta_1$  integrin and fibronectin (FN) bond, known  
19 for its instrumental role in establishing new cell adhesion sites for migration. However, upregulation of the  $\alpha_5\beta_1$ -FN bond is  
20 associated with uncontrolled cell metastasis. This bond operates through catch bond dynamics, wherein the bond lifetime  
21 paradoxically increases with greater force. The mechanism sustaining the characteristic catch bond dynamics of  $\alpha_5\beta_1$ -FN  
22 remains unclear. Leveraging molecular dynamics simulations, our approach unveils a pivot-clip mechanism. Two key  
23 binding sites on FN, namely the synergy site and the RGD (arg-gly-asp) motif, act as active points for structural changes in  
24  $\alpha_5\beta_1$  integrin. Conformational adaptations at these sites are induced by a series of hydrogen bond formations and breaks  
25 at the synergy site. We disrupt these adaptations through a double mutation on FN, known to reduce cell adhesion. A  
26 whole-cell finite element model is employed to elucidate how the synergy site may promote dynamic  $\alpha_5\beta_1$ -FN binding,  
27 resisting cell contraction. In summary, our study integrates molecular and cellular-level modeling to propose that FN's  
28 synergy site reinforces cell adhesion through enhanced binding properties and a mechanosensitive pivot-clip mechanism.  
29 This work sheds light on the intricate interplay between mechanical forces and cell-matrix interactions, contributing to our  
30 understanding of cellular behaviors in physiological and pathological contexts.

SIGNIFICANCE  $\alpha_5\beta_1$  integrin serves as a crucial mediator of cell-matrix adhesion and has garnered attention as a target for impeding cancer metastasis. Despite its importance, the mechanism underlying the formation of a catch bond between  $\alpha_5\beta_1$  integrin and its primary ligand, fibronectin, has remained elusive. Our study aims to address this gap by proposing a pivot-clip mechanism. This mechanism elucidates how  $\alpha_5\beta_1$  integrin and fibronectin collaboratively reinforce cell adhesion through conformational changes induced by the dynamic interaction of a key binding motif, known as the synergy site.

## 31 INTRODUCTION

32 Adhesion bonds enable cells to interact dynamically with their surrounding environment, orchestrating the regulation of essential  
33 cellular processes such as proliferation, differentiation, and apoptosis (1–5). Integrins are transmembrane, heterodimeric  
34 proteins that play an important role in cell adhesion by tethering the inside and outside of the cell via binding partners in  
35 the extracellular matrix (ECM) (6).  $\alpha_5\beta_1$  integrin is one of 24 integrin heterodimers present in mammals (4) and mediates  
36 cell-tissue homeostasis by binding to its primary ligand, fibronectin (FN) (7, 8).  $\alpha_5\beta_1$  and FN are linked together at the RGD  
37 (Arg-Gly-Asp) motif and stabilized by the eight-amino-acid-long DRVPHSRN synergy site on FN (9), allowing extracellular  
38 and cytoplasmic forces to be transmitted across the cell membrane. The accumulation of  $\alpha_5\beta_1$ -FN bonds form the basis for

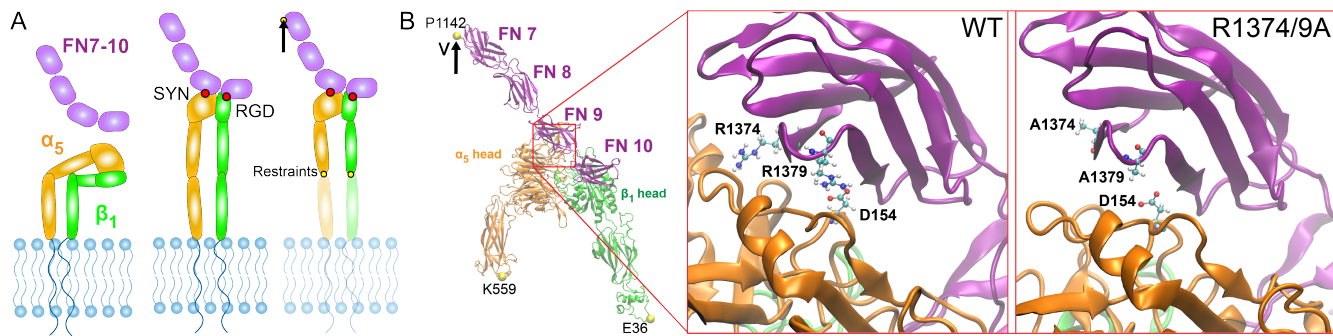


Figure 1: A) Schematics of  $\alpha_5\beta_1$  integrin in its bent-closed, inactive state with FN fragment 7-10 unbounded (left), extended-active state in complex with FN (middle), and under an applied load (right). B) The crystal structure of  $\alpha_5\beta_1$ -FN with the individual integrin heads and FN fragments labeled. The MD simulations applied a velocity to the P1142 residue while restraining K559 and E36. Zoomed in region shows wildtype synergy site with R1374 and R1379 (left) and double mutated R1374/9A synergy site (right). D154 binds to R1379 and is shown as a reference. SYN: synergy site. RGD: arg-gly-asp.

nascent cell adhesion and cell motion. Beyond  $\alpha_5\beta_1$ -FN's role in maintaining cell-tissue homeostasis, it has been implicated as a potential therapeutic target for cancer (10–12). For example, dysfunctional and overexpressed integrin bonds are markers of uninhibited cancer cell migration (13, 14). As such, numerous antagonists have been developed to attenuate integrin bonds, aiming to impede the invasion of multiple cancer cell types. Despite considerable efforts, these antagonists have faced challenges, demonstrating limited success in effectively preventing cancer cell invasion. (15, 16). Therefore, a better understanding of the biophysical nature of the  $\alpha_5\beta_1$ -FN bond is needed to reveal mechanisms that can be exploited to target metastasis.

$\alpha_5\beta_1$  integrin creates a catch bond with FN (9, 17, 18), which is a type of bond that increases in lifetime with greater applied force. The  $\alpha_5\beta_1$ -FN catch bond allows for strong adhesion at the leading edge of a migrating cell and a steady release of the bond at the cell's trailing end. Catch bonds have inspired development of synthetic catch bonds for manufacturing resilient materials (19–21). However, the mechanisms involved in the  $\alpha_5\beta_1$ -FN catch bond's ability to maintain its characteristic strength is unknown. Understanding the underlying mechanism of  $\alpha_5\beta_1$ -FN catch bond resilience could identify structural protein characteristics that can be targeted to arrest cancer cells through substrate or protein modifications. Moreover, structural dynamics that enable catch bond behavior may inspire development of resistant nanomaterials with self strengthening properties.

Ideally, the  $\alpha_5\beta_1$ -FN catch bond could be imaged while an applied force is applied with a single-molecule testing setup (e.g., optical trap or magnetic tweezers). However, current atomic-resolution molecular imaging techniques, like cryo-EM and x-ray crystallography, require immobilizing the protein, making visualization of *in situ* structural changes of  $\alpha_5\beta_1$ -FN challenging. In light of these experimental limitations, steered molecular dynamics (MD) simulations have been used to visualize protein conformational changes over time (22, 23).

Given  $\alpha_5\beta_1$ -FN's critical role in mechanosensing via its elusive catch bond dynamics, we used steered MD simulations to visualize the motion of  $\alpha_5\beta_1$ -FN when acted on by an external load. We introduce a "pivot-clip" mechanism to model the  $\alpha_5\beta_1$ -FN's catch bond-like behavior, where the RGD motif acts as a stable pivot for FN about  $\beta_1$  integrin and the synergy site acts as a force-strengthening clip connecting FN to  $\alpha_5$ . Past experiments demonstrated that mutating the synergy site diminishes catch bond behavior and weakens whole-cell and single molecule adhesion to  $\alpha_5\beta_1$  (18, 24). Even so, a lack of the synergy site does not significantly limit cell traction on a 2D substrate (25). To explain how the synergy site may promote  $\alpha_5\beta_1$ -FN binding while maintaining cell traction, we developed a 2D finite element (FE) model. Based on our MD and FE models, we present a theory that the synergy site in FN reinforces cell adhesion via stronger binding affinity and a mechanosensitive pivot-clip mechanism.

## 66 MATERIALS AND METHODS

### 67 Steered Molecular Dynamics Simulations

Constant velocity, all-atom steered MD simulations of the ectoplasmic  $\alpha_5\beta_1$ -FN complex were run in GROMACS 2020.4 (26). The 7NWL crystal structure file of the  $\alpha_5\beta_1$ -FN complex with the TS2/16 Fv-clasp was downloaded from the protein data bank. The  $\alpha_5\beta_1$  integrin head domain and the FN type III fragment 7-10 were isolated using PyMOL (27). We used MODELLER 10.4 (28) to impose a virtual R1374/9A double mutation, switching the arginine residues in positions 1374 and 1379 in FN to alanine (Figure 1B).

Wildtype and mutated structures were solvated in a TIP3P water box (18nm x 45nm x 19nm) with 0.15 mM NaCl. Energy

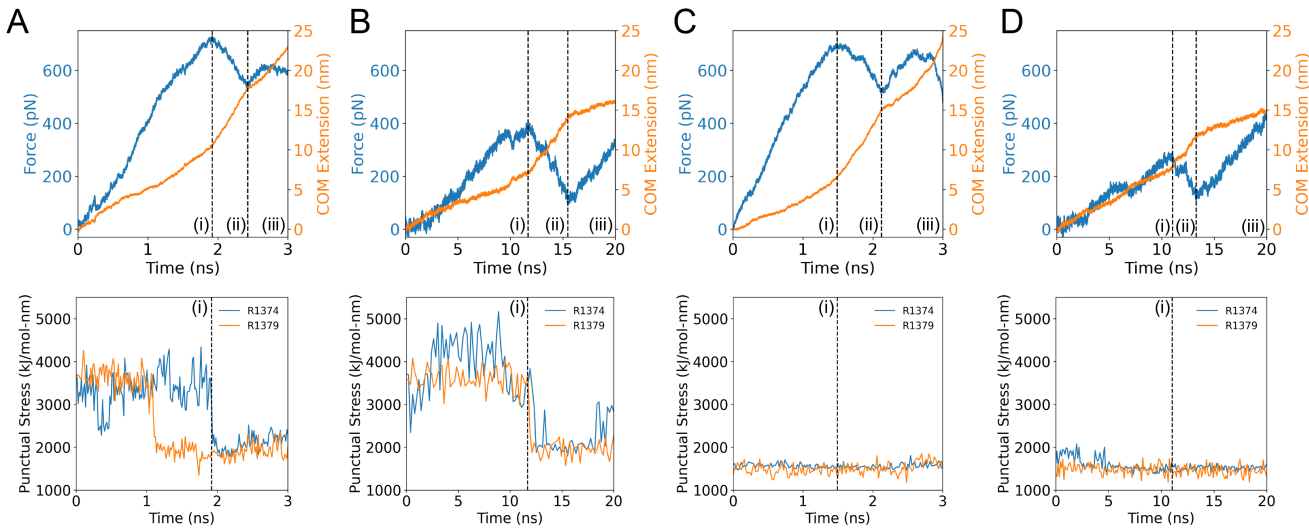


Figure 2: Force and COM extension over time plotted over punctual stress at R1374/1379 of the synergy site for A) 10nm/ns wildtype  $\alpha_5\beta_1$ -FN, B) 1nm/ns wildtype  $\alpha_5\beta_1$ -FN, C) 10nm/ns R1374/9A  $\alpha_5\beta_1$ -FN, and D) 1nm/ns R1374/9A  $\alpha_5\beta_1$ -FN. Positions (i), (ii), and (iii) correspond to the time at the peak force, local minimum, and final frame, respectively.

74 was minimized for 15k steps with the steepest gradient descent algorithm, followed by an equilibration sequence of a 1ns NVT  
 75 simulation at 310K followed by a 10ns NPT simulation at 1 bar and 310K, per physiological conditions. Equilibration was  
 76 verified by ensuring that the RMSD of the fully unrestrained complexes (Figure S1) were within 0.3nm resolution of cryoEM.

77 The K559 and E36 residues at the proximal ends of the integrin headpieces were then restrained. P1142 at the distal  
 78 end of the FN fragment was pulled at 10 and 1nm/ns using a 50kJ/mol/nm spring with an umbrella potential for 3ns and  
 79 20ns, respectively. The steered MD simulations used a 2fs timestep. We visualized the crystal structures and MD simulation  
 80 trajectories using Visual Molecular Dynamics (VMD) 1.9.4a (29). All parameters for the MD simulations are available in  
 81 the supplementary materials (Table S1). The force and extension at  $\alpha_5\beta_1$ -FN's center-of-mass were derived directly from the  
 82 output files from Gromacs. The extension was measured as the displacement of the  $\alpha_5\beta_1$ -FN's center-of-mass (COM) with  
 83 respect to the first simulation frame. The radius of gyration of the  $\alpha_5$  and  $\beta_1$  heads was measured using the built-in Gromacs  
 84 function, gmx gyrate. Distances between key bonds at R1374 and R1379 were calculated by averaging the distance between  
 85 atom pairs that could form hydrogen bonds using the VMD bond select and graph tool. We used a distance cutoff of 0.35nm  
 86 (3.5 Angstrom) and donor-hydrogen-acceptor angle cutoff of 30 in VMD to detect hydrogen bonds.

## 87 Force Distribution Analysis

88 Time-resolved force distribution analysis (trFDA) was used to measure the punctual stresses based on the Coulombic interactions  
 89 at all residues across all simulation time steps (30). The punctual stress is the absolute value of scalar pairwise forces exerted on  
 90 each residue. Normally, stress would be in units of energy. However, the developers of punctual stress defined it as "force on  
 91 a dimensionless point" which uses units of force (kJ/mol-nm). We opted to use this definition of punctual stress to remain  
 92 consistent with past studies. Parameters for the trFDA are available in the supplementary materials (Table S2).

## 93 Whole-cell Finite Element Model

94 We used a whole-cell FE model to calculate the  $\alpha_5\beta_1$ -FN concentration and force in a wildtype and mutant cell. We have  
 95 previously modeled the cell-substrate interface using a whole-cell FE model; we refer the reader to that publication for the full  
 96 set of model equations (23). In the present work, we introduced key changes to the catch bond model. We modeled the cell as a  
 97 2D elastic disk with neo-Hookean constitutive material properties on a rigid substrate,

$$\sigma_c^{\text{pas}} = \mu_c \mathbf{b}_c - p_c \mathbf{I}, \quad (1)$$

98 where  $\sigma_c^{\text{pas}}$  is the passive cell stress. The cell shear modulus is,  $\mu_c=1\text{kPa}$  (31, 32). The deformation was characterized by  
 99 the left Cauchy-Green tensor  $\mathbf{b}_c$ . The pressure  $p_c$  was computed from plane stress boundary conditions.

100 An isotropic active stress field was applied inside the cell to model cell contractility,

$$\sigma_c^{\text{act}} = t_{\text{myo}} \mathbf{I}, \quad (2)$$

101 where  $\sigma_c^{\text{act}}$  is the active cell stress due to an actomyosin traction,  $t_{\text{myo}}$  in Pa (32, 33):

$$t_{\text{myo}} = \begin{cases} 100t & 0 < t < 2 \\ 200 & 2 \leq t \leq 30 \end{cases} \quad (3)$$

102 where  $t$  is the simulation time.

103 We used an existing catch bond model of adhesion to calculate the force-dependent concentration of  $\alpha_5\beta_1$ -FN bonds per  
104 node in the FE mesh (34–37). The catch model assumed that the  $\alpha_5\beta_1$ -FN complexes behave as parallel springs that connect  
105 and disconnect to the substrate based on an association constant,  $K_{\text{on}}$  and on a force dependent dissociation constant,  $K_{\text{off}}$ ,  
106 respectively.

$$K_{\text{off}} = K_a e^{\frac{f_{\text{int}}}{F_a}} + K_b e^{-\frac{f_{\text{int}}}{F_b}}, \quad (4)$$

107 where  $K_a$ ,  $F_a$ ,  $K_b$ , and  $F_b$  are fitted parameters (Table S3) adapted from Bidone et al (37) and Takagi et al (38).  $f_{\text{int}}$  is  
108 the magnitude of the force per  $\alpha_5\beta_1$ -FN bond. The force vector per bond, ( $\mathbf{f}_{\text{int}}$ ), is computed via the  $\alpha_5\beta_1$ -FN spring constant  
109  $k_{\text{int}} = 0.5\text{pN/nm}$  (17) and the spring extension vector  $\mathbf{u}_{\text{int}}$ :

$$\mathbf{f}_{\text{int}} = k_{\text{int}} \mathbf{u}_{\text{int}}. \quad (5)$$

110 The force per node,  $\mathbf{f}_{i,\text{node}}$  is related to the dimensionless concentration of  $\alpha_5\beta_1$ -FN bonds  $C$  with respect to the maximum  
111 bond density  $\rho_{i,\text{max}} = 100\mu\text{m}^2$  (39), and the local adhesion area  $A$  at that node,

$$\mathbf{f}_{i,\text{node}} = C \rho_{i,\text{max}} A \mathbf{f}_{\text{int}}. \quad (6)$$

112 At any node,  $i$  given the previous value of the bond concentration,  $C$ , the updated bond concentration  $C_{t+\Delta t}$  at each  
113 progressive time step is

$$C_{t+\Delta t} = C(1 - K_{\text{off}} \Delta t) + K_{\text{on}} \Delta t (1 - C). \quad (7)$$

114 Note that the updated eq. (7) is based on treating the bond kinetics in the limit of an ordinary differential equation discretized  
115 in time with an explicit Euler scheme.

116 The internal force balance for the cell includes the elastic cell deformation ( $\sigma_c^{\text{pas}}$ ) and the active cell contractile stress ( $\sigma_c^{\text{act}}$ ):

$$\nabla \cdot \sigma_c = \rho_c \mathbf{a}_c, \quad (8)$$

117 in which  $\sigma_c = \sigma_c^{\text{pas}} + \sigma_c^{\text{act}}$  is the total cell stress,  $\rho_c = 1000\text{kg/m}^3$  is the cell density (40) and  $\mathbf{a}_c$  is the cell acceleration.

118 The strong forms of the elastodynamic equation 8 has boundary conditions of the form  $\sigma \cdot \mathbf{n} = \mathbf{t}$  on boundary  $\Gamma_c$ , i.e.  
119 traction free boundary conditions. The internal forces were computed through the weak form. Briefly, we multiplied equation 8  
120 by test function,  $v$ , integrated over a domain  $\Omega_c$  of thickness  $1\mu\text{m}$ , and applied divergence theorem to get the following weak  
121 form for the cell.

$$-\int_{\Omega_c} \sigma_c : \delta \mathbf{d}_c \, d\Omega_c + \int_{\Gamma_c} \mathbf{t}_c \cdot \delta \mathbf{v}_c \, dA_c = -\mathbf{R}_c + \mathbf{f}_{c,\text{ext}} = \int_{\Omega_c} \rho \mathbf{a}_c \, d\Omega_c, \quad (9)$$

122 The  $\delta \mathbf{d}$  is the variation of the symmetric velocity gradient, i.e. virtual work by moving each node by an independent  
123 variation  $\delta v$ .  $\mathbf{R}$  is the residual (internal forces) and the external force acting at a node of the cell mesh is:

$$\mathbf{f}_{c,\text{ext}} = \mathbf{f}_{i,\text{node}} + \mathbf{f}_d + \mathbf{f}_k + \mathbf{f}_{ac} + \mathbf{f}_A, \quad (10)$$

124 where  $\mathbf{f}_{i,\text{node}}$  is the force due to  $\alpha_5\beta_1$ -FN at each node,  $\mathbf{f}_d$  is viscous drag,  $\mathbf{f}_k$  is curvature regularization,  $\mathbf{f}_{ac}$  is a random  
125 fluctuation at the cell boundary from actin polymerization, and  $\mathbf{f}_A$  is an area penalty to counteract cell contractility.

126 The mesh was updated by a dynamic explicit mesh generator, El Topo (41), during the simulation run. The explicit mid-point  
127 rule was used for time integration of the second order system of equations to update nodal velocities and positions. The  
128 whole-cell FE simulation ran with a time step of  $50\mu\text{s}$  over the course of an assigned time of  $t_{\text{sim}} = 30\text{s}$ . There were a total  
129 of three simulation runs per R1374/9A mutant and wildtype catch bond condition, respectively. The three simulation bond  
130 concentration and force outputs were time-averaged per condition.

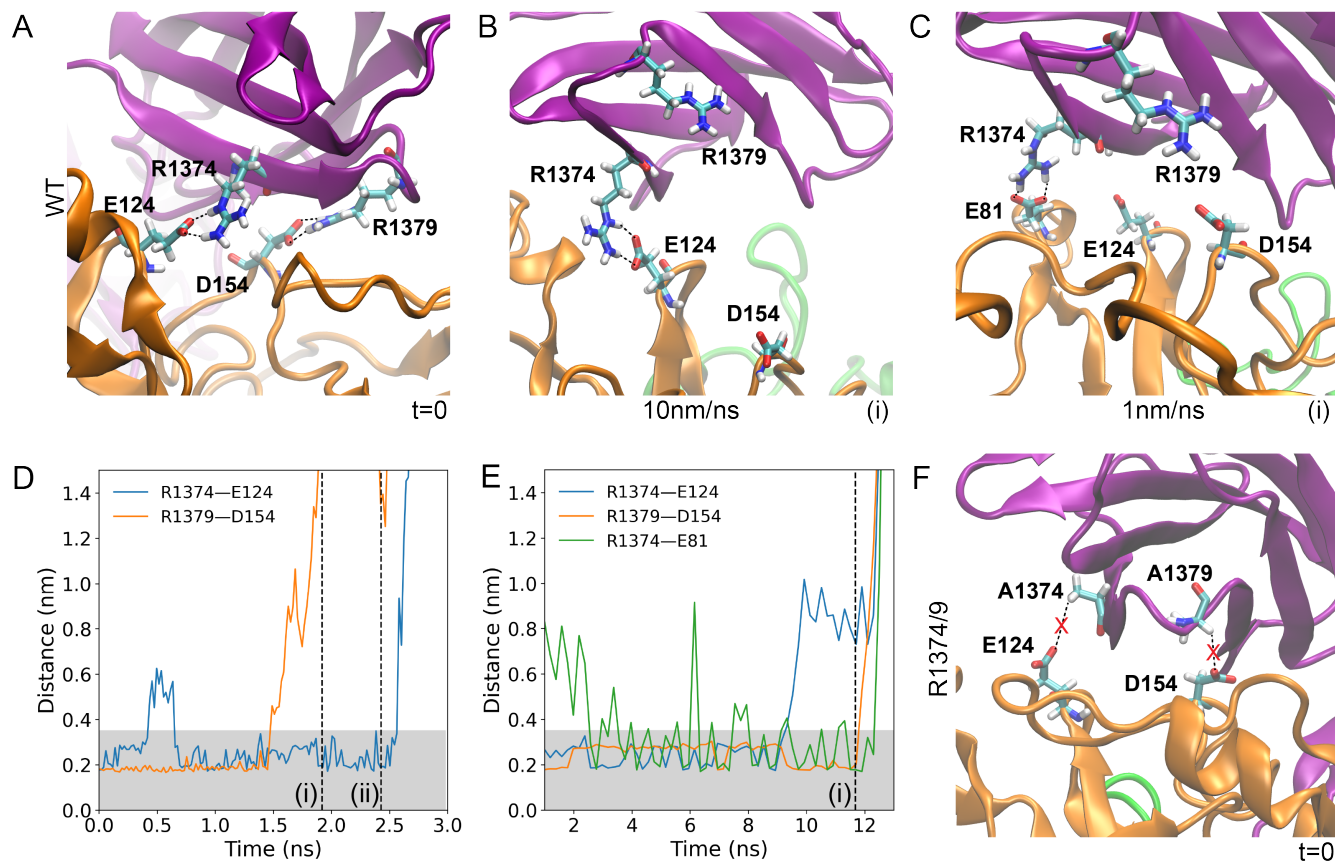


Figure 3: A) Interactions between R1374—E124 and R1379—D154 at the beginning of the wildtype simulations. B) At the force peak of the 10nm/ns wildtype simulation, the R1379—D154 salt bridge was broken but R1374—E124 remained. C) At the force peak of the 1nm/ns wildtype simulation, the R1379—D154 salt bridge was broken and R1374 formed a new hydrogen bond with E81. D) Distance between R1374—E124 and R1379—D154 for the 10nm/ns wildtype simulation. E) Distance between R1374—E124, R1379—D154, and R1374—E81. Shaded regions indicate 0.35nm, or the assumed approximate length for a hydrogen bond. The vertical dashed line is the time point of the force peak. F) The R1374/9A double mutation separated the A1374—E124 and A1379—D154 bonds to over 0.65nm, preventing hydrogen bond formation.

## RESULTS AND DISCUSSION

### FN9- $\alpha_5$ disengagement coincides with synergy site deactivation

We analyzed force-extension in conjunction with punctual stress to determine the role of the synergy site in FN9- $\alpha_5$  disengagement. The initial force-extension curve of the wildtype  $\alpha_5\beta_1$ -FN structure followed a linear response for both 10 and 1 nm/ns pull rates until peaking at 729pN and 462pN, respectively (Figure 2A and B). The peak forces coincided with sharp decreases in the punctual stress at the synergy site, namely at sites R1374 and R1379 in FN9. R1379 has been shown to be connected to D154 in the  $\alpha_5$  head via a salt bridge (13). However, R1374 has not been previously observed to be actively linked to  $\alpha_5$ . At both pull rates, R1374 retained higher punctual stresses than R1379, but the sequence of disengagement was dependent on the pull rate. Under the faster pull rate condition, the salt bridge was disrupted prior to a reduction in force on  $\alpha_5\beta_1$ -FN and punctual stress at R1374. This indicated that while the load on FN was sufficient to overcome the energetic barrier to break the salt bridge connecting FN to  $\alpha_5$ , persistent electrostatic interaction at R1374 enabled additional force resistance. This was not observed under the slower pull rate simulation, where we noted simultaneous punctual stress reduction in R1374 and R1379 at the peak force time point. While both residues were instrumental to resisting applied load at the synergy site, faster rates that produced higher forces triggered new modes of force distribution at the residue-level. On the whole, the synergy site engagement at multiple residues, as measured by the punctual stress, reduced after the peak force.

R1374 and R1379 were the primary contributors to punctual stress at the synergy site prior to the drop in force on  $\alpha_5\beta_1$ -FN (Figure S2). In both pull rate conditions, the combined punctual stress at R1374/9 prior to the force peak was on average two

148 times higher than other synergy site residues. Due to the importance of both sites, we mutated them (R1374/9A) to evaluate  
149 their role in maintaining  $\alpha_5\beta_1$ -FN's structural response to force. At 10nm/ns, the force response of the wildtype and mutant  
150  $\alpha_5\beta_1$ -FN were similar, peaking at 729pN and 704pN, respectively (Figure 2C). However, the punctual stresses at A1374 and  
151 A1379 were 45% and 40% lower in the mutant case than the wildtype (Figure 2C and D), indicating that the mutation disrupted  
152 force transmission. Similar trends were observed in the 1nm/ns force rate condition, where the punctual stresses at A1374 and  
153 A1349 were small relative to R1374 and R1379, and the first peak force was lower in the mutant case (wildtype = 462pN,  
154 mutant = 291pN; Figure 2D).

155 Punctual stress measurements provide insight into per-residue interactions and are substantiated by atomic-level interactions.  
156 Specifically, the formation and breakage of hydrogen bonds between  $\alpha_5$  and FN9 are essential for relaying force between  
157 the two. Since high punctual stresses were observed on R1374 and R1379, we tracked bonds between R1379—D154 and  
158 R1374—E124 (Figure 3A). At both pull rates, the R1379—D154 salt bridge was broken before the maximum force was reached,  
159 while residue R1374 remained bounded to either E124 or E81 depending on the pull rate (Figure 3B and C). The measured  
160 distance between R1374—E124 was within the range of a hydrogen bond (0.35nm) after the departure of the R1379—D154  
161 bond (10nm/ns case; Figure 3D). At the slower pull rate, R1374 transitioned from E124 to E81, maintaining contact between  
162 FN9 and  $\alpha_5\beta_1$  together with R1379—D154 (Figure 3E). Both bonds then released and the force on  $\alpha_5\beta_1$ -FN consequently  
163 dropped. The R1374/9A double mutation severed the main points of contact between FN9 and  $\alpha_5\beta_1$ , pushing the distance  
164 between the residues to 0.65nm, beyond the 0.35nm hydrogen bond length cutoff (Figure 3F).

165 For all test cases, the peak forces were followed by sharp increases in extension rate, suggesting a rapid conformational  
166 change of  $\alpha_5\beta_1$ -FN (Figure 2). In the case of the wildtype 10nm/ns pull rate, the measured extension rate increased from  
167 5.10nm/ns to 14.4nm/ns. Similarly, the wildtype 1nm/ns pull rate increased in rate from 0.547nm/ns to 1.82nm/ns (Table 1).  
168 Notably, there was a mismatch between the input rate and measured rate. Steered MD simulations attempt to control the pull  
169 rate via a virtual spring connecting a dummy atom to the pulled site. While the atom moves at a constant rate, the molecule's  
170 response depends on the virtual spring deflection and local conformational changes associated with the molecule. Therefore, it  
171 is unlikely that the input pull rate matches the measured pull rate experienced by the molecule. Further, the output extension  
172 was measured as the distance traveled by  $\alpha_5\beta_1$ -FN's COM, which depends on the structural behavior.

173 Our reported forces and pull rates are many orders of magnitude higher than what has been tested using atomic force  
174 microscopy (AFM; 1 - 15  $\mu$ m/s) (42). Given our large 1.5M atom system, we compromised on the simulation time scale by  
175 applying extension rates within the bounds of past steered MD simulations of integrin (0.1 - 10 nm/ns) (22, 43). The fast  
176 extension rates contributed to simulated forces beyond what has previously been measured experimentally (single molecule  
177 rupture forces of 80-120pN) (42). Nevertheless, the difference between 10nm/ns and 1nm/ns was enough to note structural  
178 shifts in  $\alpha_5\beta_1$ -FN that enable larger force resistance due to synergy site engagement.

Table 1: Measured extension rate (nm/ns) of  $\alpha_5\beta_1$ -FN under load in reference to the (i) peak and (ii) valley force, as seen in Figure 2.

	Prior to (i)	Between (i) and (ii)	After (ii)
10nm/ns wildtype	5.10	14.4	9.21
10nm/ns R1374/9A	4.17	13.2	9.15
1nm/ns wildtype	0.547	1.82	0.546
1nm/ns R1374/9A	0.705	1.63	0.562

## 179 Conformational response of $\alpha_5$ and $\beta_1$ was hampered by lack of synergy site engagement

180 We informed the differences in force and extension rates across conditions by visualizing the structural changes of  $\alpha_5\beta_1$ -FN  
181 under both pull rates for the wildtype and mutant cases. We used the radius of gyration to quantify conformational changes  
182 within  $\alpha_5$  and  $\beta_1$  heads, with smaller radii indicating more compact proteins. In both wildtype runs, the  $\alpha_5$  head, which is  
183 connected to the synergy site on FN9, stretched further than the  $\beta_1$  head, which is connected to the RGD motif on FN10.  
184 However, pull rate affected the degree of  $\alpha_5$  stretching. The lower 1nm/ns pull rate resulted in 0.165nm increase in  $\alpha_5$ 's  
185 radius of gyration, compared to a 0.407nm increase in the 10nm/ns rate simulation (Figure 4A and B). Most of the  $\alpha_5$  head  
186 deformation resulted before the peak force and synergy site disengagement. For the respective 10nm/ns and 1nm/ns rates,  
187 97.7% and 99.0% of the max  $\alpha_5$  head deformation occurred prior to the peak force, when the synergy site loosened. From the  
188 observations of  $\alpha_5\beta_1$ -FN's quaternary structure, we noticed the  $\alpha_5$  head straightening while FN9 remained connected at the  
189 synergy site (Figure 4C). Further, at higher forces,  $\alpha_5$  underwent a greater degree of stretching and was able to resist synergy  
190 site disengagement while FN9 unfolded (Figure 4D). In contrast, lower forces seemed to encourage synergy site disengagement

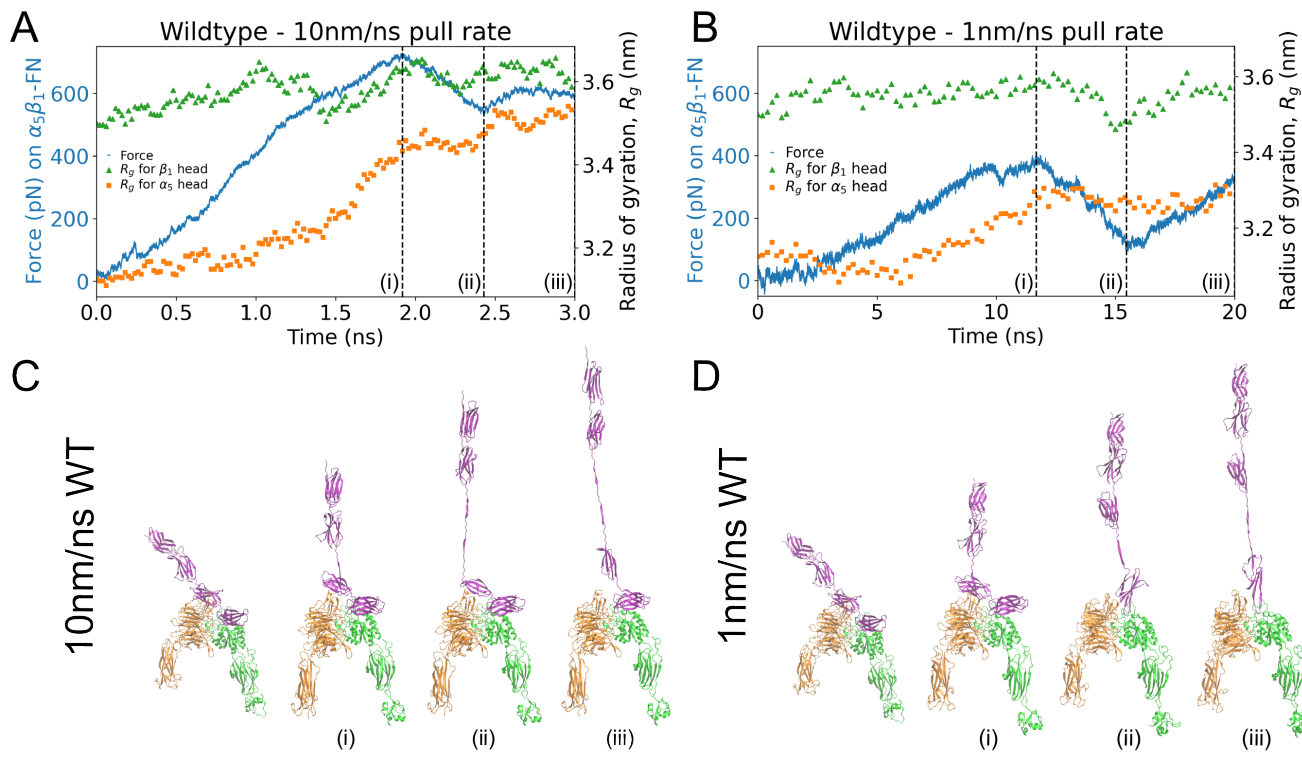


Figure 4: Force on  $\alpha_5\beta_1$ -FN and radius of gyration of  $\alpha_5$  and  $\beta_1$  head for the wildtype case pulled at A) 10nm/ns and B) 1nm/ns. Positions (i), (ii), and (iii) correspond to the time at the peak force, local minimum, and final frame. The four shown frames from the simulation correspond to the first frame, (i) peak force, (ii) local minimum, and (iii) final frame for C) 10nm/ns and D) 1nm/ns wildtype cases.

191 prior to FN unfolding. Our observation suggests that  $\alpha_5\beta_1$ -FN's catch bond dynamics may be promoted by greater synergy site  
 192 interaction in combination with  $\alpha_5$  extension to resist larger forces. The greater interaction may stem from the hydrogen bond  
 193 electrostatics at R1374 and R1379 that bridge  $\alpha_5$  to FN9 (Figure 3).

194 We tested the degree to which the synergy site contributed to structural changes in  $\alpha_5\beta_1$ -FN by mutating the site (R1374/9A)  
 195 and again measuring the radius of gyration of  $\alpha_5$  and  $\beta_1$  under an external load on FN. Surprisingly, the mutant pulled at  
 196 10nm/ns still resulted in conformational changes of the  $\alpha_5$  head, with the radius of gyration increasing by 0.266nm. However,  
 197 this was less than the 0.407nm increase observed in the wildtype (Figure 5A). Further, the mutant pulled at the slower 1nm/ns  
 198 showed virtually no deformation of  $\alpha_5$  or  $\beta_1$  (Figure 5B). Investigating the quaternary structure of the mutant revealed that FN9  
 199 was separated immediately from  $\alpha_5$  (Figure 5C and D). As the FN beta sheets stacked vertically in alignment with the pulling  
 200 direction, the force increased and peaked as soon as FN10 began to unfold. For all simulations, the  $\beta_1$  head kept a more stable  
 201 conformation, maintaining its radius of gyration within 0.12nm.

202 Our observations of the mutant trajectories support the conjecture that the synergy site may be responsible for reinforcing  
 203 integrin engagement (13, 24). Our results also imply that force between the synergy site and  $\alpha_5$  integrin head may be necessary  
 204 to induce conformational changes in both integrin heads. Overall, our results highlight the importance of the synergy site clip in  
 205 stabilizing and reinforcing the  $\alpha_5\beta_1$ -FN bond after initial catch bond formation, which has also been previously suggested  
 206 experimentally (9, 25, 44, 45). While cell adhesion can be negated altogether by an RGD deletion as demonstrated by spinning  
 207 disk assays, the R1374/9A double mutation reduces cell adhesion strength by around 90% (24). So, while adhesion could still  
 208 occur, the bond strength was compromised due to the synergy site mutation, which has also been shown previously through  
 209 single molecule AFM (42). Additionally, past surface plasmon resonance binding assays measure an 11-fold decrease in affinity  
 210 between  $\alpha_5\beta_1$  and R1374A FN compared to wildtype (38). Clearly, the role of the synergy site in maintaining a firm adhesion  
 211 cannot be understated. Here, we propose how the synergy site may give rise to specific molecular states of  $\alpha_5\beta_1$  integrin and  
 212 unfolding patterns of FN that show how adhesion reinforcement may occur in the presence of force. While our study highlighted  
 213 the reinforcing role of the synergy site at the molecular scale, we also sought to explore how this adhesion reinforcement may  
 214 dynamically manifest at the whole cell scale.

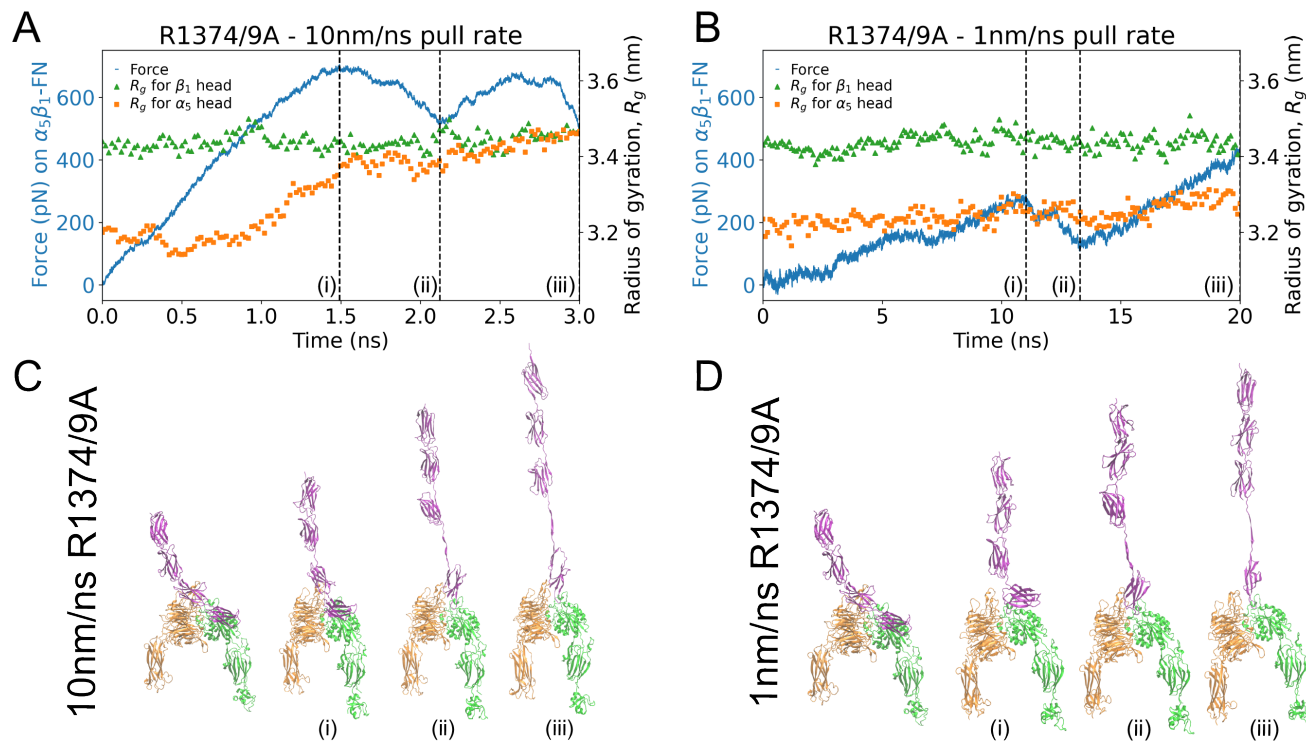


Figure 5: Force on mutated  $\alpha_5\beta_1$ -FN and radius of gyration of  $\alpha_5$  and  $\beta_1$  head pulled at A) 10 nm/ns and B) 1 nm/ns. For both figures, positions (i), (ii), and (iii) correspond to the time at the peak force, local minimum, and final frame. First frame of the simulation and three simulation frames corresponding to (i) peak force, (ii) local minimum, and (iii) final frame for C) 10 nm/ns and D) 1 nm/ns mutant cases.

## 215 Synergy site presence led to adhesion reinforcement by recruiting $\alpha_5\beta_1$ integrin

216 We employed a whole-cell FE model that analyzed the adhesion interface that contained  $\alpha_5\beta_1$ -FN bonds under an isotropic cell  
 217 contraction that drove bond extension (Figure 6A). Our simple model demonstrated an adaptive reinforcement of collective  
 218  $\alpha_5\beta_1$ -FN bonds due to the stronger binding affinity afforded by the synergy site. We modified the parameters for the  $\alpha_5\beta_1$ -FN  
 219 binding kinetics (Table S3) to produce bond lifetime curves for the wildtype bond and R1374/9A mutant (Figure 6B). The  
 220 differences in parameters between the two bond types resulted in an 11-fold decrease in  $\alpha_5\beta_1$ -FN bond concentration (Figure  
 221 6C), but no increase in equilibrium force (Figure 6D). The areas of high concentrations and high forces are present at the  
 222 periphery of the cell during contraction (Figures 6E and 6F), which has been shown by 2D Fluorescence Resonance Energy  
 223 Transfer (FRET) and traction force microscopy (TFM) assays (25). Notably, mutant bonds compensate for the lack of number of  
 224 bonds by sustaining more of the cell's contractile load. The higher recruitment of wildtype bonds distributes the forces more  
 225 evenly across the cell.

226 Our whole-cell FE model sheds light on the dynamic force balance at short timescales that are not as apparent experimentally.  
 227 TFM of cells plated on 2D substrates have shown that cell contraction and individual bond force were not altered due to an  
 228 absence of the synergy site (25, 45). Our model used the same 200Pa cell contraction across both conditions, but showed a stark  
 229 difference in how the adhesion forces are handled by the bonds. Namely, while forces eventually equalized between mutant and  
 230 wildtype conditions, we observed an initial dynamic adjustment of high forces at the cell boundary for mutant bonds (Figure  
 231 6F). Specifically, average forces measured from mutated bonds peaked at 7 pN, while wildtype bonds peaked at 3 pN; both  
 232 average bond forces were within the previously measured 1-7 pN range (25). A body of work has shown the reduction in cell  
 233 adhesion strength at the single molecule and whole cell scale due to a lack of synergy site engagement (24, 25, 42, 45). In spite  
 234 of the reduced bond strength, our work showed that the binding affinity gain due to the presence of the synergy led to a more  
 235 stable, dynamic force balance across the  $\alpha_5\beta_1$ -FN bonds on the cell surface.

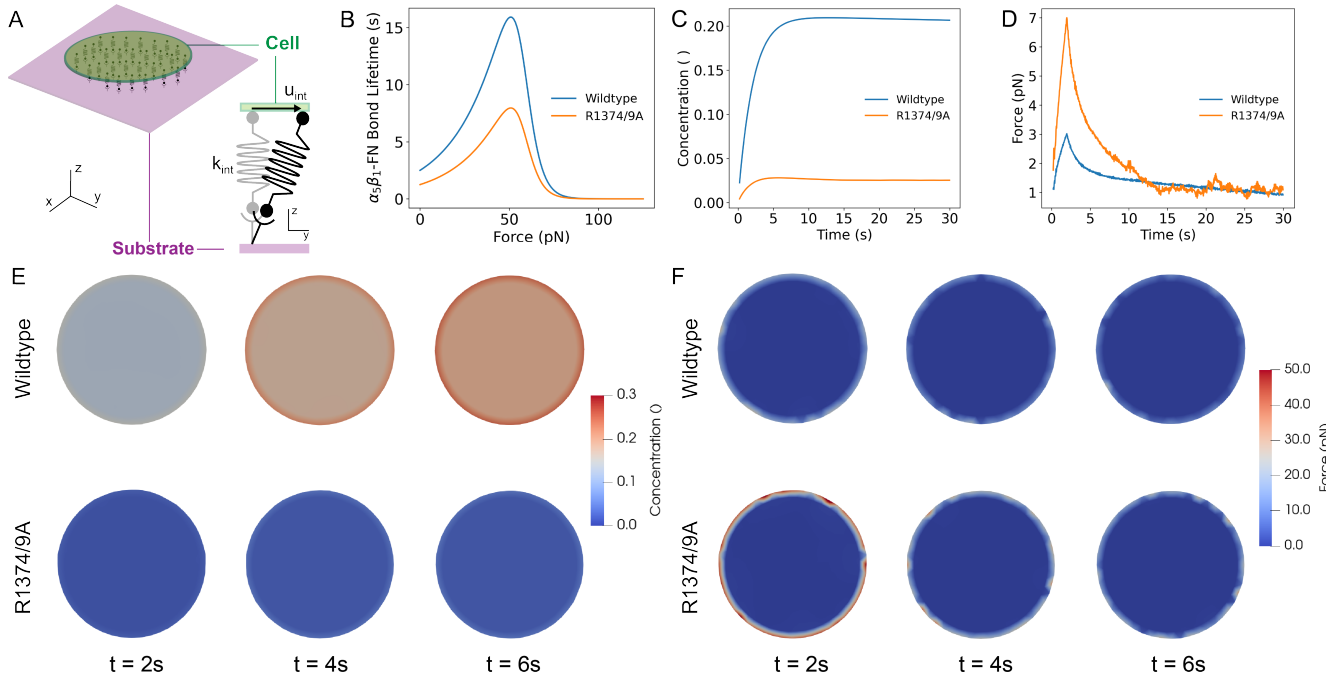


Figure 6: A) Schematic of whole-cell interface model that assumes that integrin behaves as a spring that is stretched due to cell contraction. B) Catch bond model:  $\alpha_5\beta_1$ -FN bond lifetime versus applied force for wildtype (adapted from (37, 38)). C) Concentration over time of wildtype and mutant  $\alpha_5\beta_1$ -FN. D) Force over time of wildtype and mutant  $\alpha_5\beta_1$ -FN. E) Frames at times 2, 4, and 6s indicating the concentration of  $\alpha_5\beta_1$ -FN bonds across the cell-substrate interface during a 200Pa uniform contraction. F) Frames at times 2, 4, and 6s indicating the distribution of  $\alpha_5\beta_1$ -FN bond force across the cell-substrate interface during a 200Pa uniform contraction.

## 236 Pivot-clip mechanism of $\alpha_5\beta_1$ -FN as a model for cell adhesion reinforcement

237 The mechanosensitive pivot-clip mechanism provides a model to consider how the  $\alpha_5\beta_1$ -FN catch bond reinforces cell adhesion  
 238 across molecular and cell scales under cell-matrix forces (Figure 7A). At both pull rates tested in the wildtype  $\alpha_5\beta_1$ -FN bonds,  
 239 the unbinding of FN9- $\alpha_5$  coincided with a plateauing of  $\alpha_5$  extension and a small compression of  $\beta_1$  (Figure 4A and B). With  
 240 the link between FN9- $\alpha_5$  broken, FN10 was free to rotate about the RGD motif on  $\beta_1$  (Figure 4C and D). The FN10 rotation  
 241 about the RGD site was maintained in the mutant runs while diminishing the extension of  $\alpha_5$ , especially in the high pull rate  
 242 condition (Figure 5). Based on the structural changes observed on  $\alpha_5$  and  $\beta_1$ , the synergy site clipped the  $\alpha_5$  head to FN9 while  
 243 the RGD motif on  $\beta_1$  acted as a pivot for FN10 (Figure 7B). The degree to which the clip engaged was force dependent, with  
 244 higher forces leading to greater clip engagement due to hydrogen bond rearrangement. While it has been known that the synergy  
 245 site plays a role in catch bond dynamics (17, 24), the heightened clip engagement under higher forces could be one mechanism  
 246 by which the synergy site enables catch bond dynamics at the molecular scale. Moreover, we showed that the synergy site  
 247 contributed to conformational changes of  $\alpha_5\beta_1$  integrin that has been hypothesized to result in downstream mechanosignaling  
 248 via focal adhesion kinase phosphorylation (13, 24, 35).

249 In the context of outside-in signaling, the  $\alpha_5\beta_1$ -FN pivot-clip mechanism demonstrates how the synergy site may play a role  
 250 in moving both integrin heads, potentially leading to cell-scale changes. According to the outside-in activation model, integrins  
 251 maintain a bent-closed, low affinity state before undergoing a conformational change to an extended, active conformation  
 252 upon encountering an ECM ligand (Figure 1A) (46–48). In contrast, the inside-out model proposes that the adaptor protein  
 253 talin would bind to the cytoplasmic tail of integrin, allowing it to activate and subsequently bind to its ligand (46–48). While  
 254 the current hypothesis states that binding between FN and  $\alpha_5\beta_1$  triggers an opening of integrin's cytoplasmic tails leading  
 255 to an accumulation of adaptor proteins that resist cell-matrix forces (Figure 7A), further studies are needed to elucidate the  
 256 mechanism behind integrin activation. Multiple steered MD models have been employed to interrogate  $\beta_3$  integrin activation  
 257 (22, 43, 49–52), with few investigating the cytoplasmic end of  $\beta_1$  integrin (53, 54). However, to our knowledge, our approach is  
 258 unique in that we model the interface between FN and the  $\alpha_5\beta_1$  integrin heads, where forces interchange between the cell and  
 259 its matrix.

260 Our study acknowledges several limitations. Firstly, we made the assumption that the proximal ends of the integrin heads  
261 were anchored by fully extended integrin legs tightly held by tails in the cell membrane. While this assumption contributed to  
262 model stability, it is worth noting that the head-leg junction has been suggested to possess greater flexibility (13). Relaxing the  
263 constraints on the proximal ends to allow lateral movement may introduce flexibility without the added complexity of integrating  
264 the legs. Secondly, our study applied a large, vertical pulling rate. While this approach is advantageous for directly stressing the  
265 points of contact between FN and  $\alpha_5\beta_1$ , it is essential to recognize the need for changing the force vector to investigate other  
266 potential loading states, such as shear or torsion. Lastly, our focus was on a specific integrin subtype. The intricate nature of  
267 cell-matrix interactions involves multiple integrin subtypes and their respective ligands. Due to the prohibitive cost of molecular  
268 dynamics simulations, alternative approaches such as coarse-grained or agent-based models, capable of examining cell-matrix  
269 interactions at a broader systems level and over extended timescales, may be necessary.

## 270 CONCLUSION

271 This work advances our understanding of cell mechanobiology by introducing a mechanosensitive mechanism, termed pivot-clip,  
272 by which  $\alpha_5\beta_1$  integrin reinforces cell adhesion. Through physics-based simulations, we shed light on a key biophysical  
273 exchange between the cell and ECM that underpin many cellular behaviors that drive physiology and pathology. Critically, we  
274 also demonstrated essential binding domains that promote catch bond dynamics in the context of cell-matrix mechanosensing.  
275 Looking forward, we envision elucidating how the force-dependent, pivot-clip mechanism interacts with its surrounding  
276 machinery and how it may be transformed via novel therapeutics. As our understanding of cell adhesion progresses, we aim to  
277 develop informed approaches to target diseases that rely on transmitting forces via cell-matrix bonds.

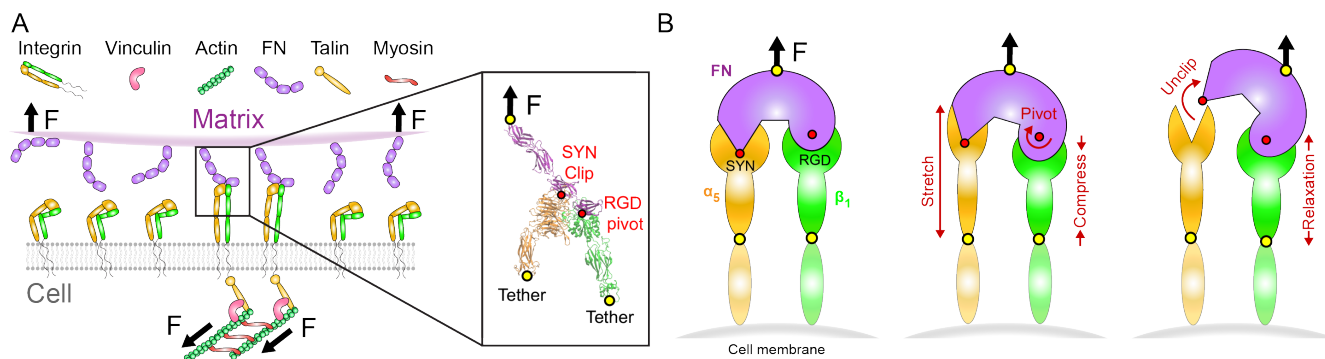


Figure 7: A)  $\alpha_5\beta_1$ -FN bridges forces between the cell and matrix, supported by cytoplasmic adaptor proteins. B) Schematics of pivot-clip mechanism. Under an applied force, the synergy site in  $\alpha_5$  and RGD motif in  $\beta_1$  act as a clip and a pivot, respectively.  $\alpha_5$  stretches, allowing FN to pivot about RGD before unclipping at the synergy site.

## 278 AUTHOR CONTRIBUTIONS

279 A.R.M., A.B.T., and M.R.K.M conceptualized and designed the research. A.R.M., A.B., and W.W. performed the research and  
280 analyzed data. A.R.M. wrote the manuscript. G.D.O., A.B.T., and M.R.K.M supervised the research and edited the manuscript.

## 281 ACKNOWLEDGMENTS

282 This research used Expanse at San Diego Supercomputer Center through allocation MCB100146 from Advanced Cyberinfrastr-  
283 tructure Coordination Ecosystem: Services & Support (ACCESS) super-computing facilities, supported by the National Science  
284 Foundation (NSF) (Grant Nos. 2138259, 2138286, 2138307, 2137603, and 2138296). A.R.M. was supported by the Ford  
285 Predoctoral Fellowship, UC Berkeley College of Engineering Robert N. Noyce Fellowship, and Hearts to Humanity Eternal  
286 Research Fellowship. A.B. was supported by the National Institute of Health Maximizing Access to Research Careers T34  
287 Award. W.W. was supported by the NSF Research Experience for Undergraduates via the Transfer-to-Excellence Program at  
288 University of California, Berkeley. A.B.T was supported by the UC Berkeley Miller Institute for Basic Research in Science.  
289 We thank members of the Molecular Cell Biomechanics and Berkeley Biomechanics Labs for fruitful discussions that led to  
290 the improvement of this manuscript. Special thank you to Mohammad Khavani for his suggestions to improve the molecular  
291 dynamics simulations.

## 292 REFERENCES

- 293 1. Damiano, J. S., A. E. Cress, L. A. Hazlehurst, A. A. Shtil, and W. S. Dalton, 1999. Cell adhesion mediated drug resistance  
294 (CAM-DR): role of integrins and resistance to apoptosis in human myeloma cell lines. *Blood, the Journal of the American  
295 Society of Hematology* 93:1658–1667.
- 296 2. Bachmann, M., S. Kukkurainen, V. P. Hytönen, and B. Wehrle-Haller, 2019. Cell adhesion by integrins. *Physiological  
297 reviews* 99:1655–1699.
- 298 3. Lee, M. H., P. Ducheyne, L. Lynch, D. Boettiger, and R. J. Composto, 2006. Effect of biomaterial surface properties on  
299 fibronectin- $\alpha 5\beta 1$  integrin interaction and cellular attachment. *Biomaterials* 27:1907–1916.
- 300 4. Hynes, R. O., 2002. Integrins: bidirectional, allosteric signaling machines. *cell* 110:673–687.
- 301 5. Ross, T. D., B. G. Coon, S. Yun, N. Baeyens, K. Tanaka, M. Ouyang, and M. A. Schwartz, 2013. Integrins in  
302 mechanotransduction. *Current opinion in cell biology* 25:613–618.
- 303 6. Cutler, S. M., and A. J. García, 2003. Engineering cell adhesive surfaces that direct integrin  $\alpha 5\beta 1$  binding using a  
304 recombinant fragment of fibronectin. *Biomaterials* 24:1759–1770.
- 305 7. Scheiblin, D. A., J. Gao, J. L. Caplan, V. N. Simirskii, K. J. Czymmek, R. T. Mathias, and M. K. Duncan, 2014. Beta-1  
306 integrin is important for the structural maintenance and homeostasis of differentiating fiber cells. *The international journal  
307 of biochemistry & cell biology* 50:132–145.
- 308 8. Humphrey, J. D., E. R. Dufresne, and M. A. Schwartz, 2014. Mechanotransduction and extracellular matrix homeostasis.  
309 *Nature reviews Molecular cell biology* 15:802–812.
- 310 9. Benito-Jardón, M., S. Klapproth, I. Gimeno-LLuch, T. Petzold, M. Bharadwaj, D. J. Müller, G. Zuchtriegel, C. A. Reichel,  
311 and M. Costell, 2017. The fibronectin synergy site re-enforces cell adhesion and mediates a crosstalk between integrin  
312 classes. *Elife* 6:e22264.
- 313 10. Hou, J., D. Yan, Y. Liu, P. Huang, and H. Cui, 2020. The roles of integrin  $\alpha 5\beta 1$  in human cancer. *Oncotargets and therapy*  
314 13329–13344.
- 315 11. Zhao, X.-K., Y. Cheng, M. Liang Cheng, L. Yu, M. Mu, H. Li, Y. Liu, B. Zhang, Y. Yao, H. Guo, et al., 2016. Focal  
316 adhesion kinase regulates fibroblast migration via integrin beta-1 and plays a central role in fibrosis. *Scientific reports*  
317 6:19276.
- 318 12. Cao, L., J. Nicosia, J. Larouche, Y. Zhang, H. Bachman, A. C. Brown, L. Holmgren, and T. H. Barker, 2017. Detection of  
319 an integrin-binding mechanoswitch within fibronectin during tissue formation and fibrosis. *ACS nano* 11:7110–7117.
- 320 13. Schumacher, S., D. Dedden, R. V. Nunez, K. Matoba, J. Takagi, C. Bierbaum, and N. Mizuno, 2021. Structural insights  
321 into integrin  $\alpha 5\beta 1$  opening by fibronectin ligand. *Science Advances* 7:eabe9716.
- 322 14. Kechagia, J. Z., J. Ivaska, and P. Roca-Cusachs, 2019. Integrins as biomechanical sensors of the microenvironment. *Nature  
323 Reviews Molecular Cell Biology* 20:457–473.
- 324 15. Schaffner, F., A. M. Ray, and M. Dontenwill, 2013. Integrin  $\alpha 5\beta 1$ , the fibronectin receptor, as a pertinent therapeutic target  
325 in solid tumors. *Cancers* 5:27–47.
- 326 16. Cox, D., M. Brennan, and N. Moran, 2010. Integrins as therapeutic targets: lessons and opportunities. *Nature reviews  
327 Drug discovery* 9:804–820.
- 328 17. Kong, F., A. J. García, A. P. Mould, M. J. Humphries, and C. Zhu, 2009. Demonstration of catch bonds between an integrin  
329 and its ligand. *Journal of Cell Biology* 185:1275–1284.
- 330 18. Strohmeyer, N., M. Bharadwaj, M. Costell, R. Fässler, and D. J. Müller, 2017. Fibronectin-bound  $\alpha 5\beta 1$  integrins sense  
331 load and signal to reinforce adhesion in less than a second. *Nature Materials* 16:1262–1270.
- 332 19. Dansuk, K. C., and S. Keten, 2021. Self-strengthening biphasic nanoparticle assemblies with intrinsic catch bonds. *Nature  
333 communications* 12:85.

- 334 20. Dansuk, K. C., S. Pal, and S. Keten, 2023. A catch bond mechanism with looped adhesive tethers for self-strengthening  
335 materials. *Communications Materials* 4:60.
- 336 21. Yuan, Z., X. Duan, X. Su, Z. Tian, A. Jiang, Z. Wan, H. Wang, P. Wei, B. Zhao, X. Liu, et al., 2023. Catch bond-inspired  
337 hydrogels with repeatable and loading rate-sensitive specific adhesion. *Bioactive Materials* 21:566–575.
- 338 22. Kulke, M., and W. Langel, 2020. Molecular dynamics simulations to the bidirectional adhesion signaling pathway of  
339 integrin  $\alpha V\beta 3$ . *Proteins: Structure, Function, and Bioinformatics* 88:679–688.
- 340 23. Montes, A. R., G. Gutierrez, A. Buganza Tepole, and M. R. K. Mofrad, 2023. Multiscale computational framework to  
341 investigate integrin mechanosensing and cell adhesion. *Journal of Applied Physics* 134:114702.
- 342 24. Friedland, J. C., M. H. Lee, and D. Boettiger, 2009. Mechanically activated integrin switch controls  $\alpha 5\beta 1$  function. *Science*  
343 323:642–644.
- 344 25. Chang, A. C., A. H. Mekhdjian, M. Morimatsu, A. K. Denisin, B. L. Pruitt, and A. R. Dunn, 2016. Single molecule force  
345 measurements in living cells reveal a minimally tensioned integrin state. *ACS nano* 10:10745–10752.
- 346 26. Abraham, M. J., T. Murtola, R. Schulz, S. Páll, J. C. Smith, B. Hess, and E. Lindahl, 2015. GROMACS: High performance  
347 molecular simulations through multi-level parallelism from laptops to supercomputers. *SoftwareX* 1:19–25.
- 348 27. Schrödinger, L., 2015. The PyMOL Molecular Graphics System, Version 1.8.
- 349 28. Webb, B., and A. Sali, 2016. Comparative protein structure modeling using MODELLER. *Current protocols in  
350 bioinformatics* 54:5–6.
- 351 29. Humphrey, W., A. Dalke, and K. Schulten, 1996. VMD: visual molecular dynamics. *Journal of molecular graphics*  
352 14:33–38.
- 353 30. Costescu, B. I., and F. Gräter, 2013. Time-resolved force distribution analysis. *BMC biophysics* 6:1–5.
- 354 31. Luo, Q., D. Kuang, B. Zhang, and G. Song, 2016. Cell stiffness determined by atomic force microscopy and its correlation  
355 with cell motility. *Biochimica et Biophysica Acta (BBA)-General Subjects* 1860:1953–1960.
- 356 32. Schierbaum, N., J. Rheinlaender, and T. E. Schäffer, 2019. Combined atomic force microscopy (AFM) and traction force  
357 microscopy (TFM) reveals a correlation between viscoelastic material properties and contractile prestress of living cells.  
358 *Soft Matter* 15:1721–1729.
- 359 33. Chen, C., J. Xie, L. Deng, and L. Yang, 2014. Substrate stiffness together with soluble factors affects chondrocyte  
360 mechanoresponses. *ACS applied materials & interfaces* 6:16106–16116.
- 361 34. Guo, Y., S. Calve, and A. B. Tepole, 2022. Multiscale mechanobiology: Coupling models of adhesion kinetics and nonlinear  
362 tissue mechanics. *Biophysical Journal* 121:525–539.
- 363 35. Cheng, B., W. Wan, G. Huang, Y. Li, G. M. Genin, M. R. Mofrad, T. J. Lu, F. Xu, and M. Lin, 2020. Nanoscale integrin  
364 cluster dynamics controls cellular mechanosensing via FAKY397 phosphorylation. *Science advances* 6:eaax1909.
- 365 36. Bell, G. I., 1978. Models for the specific adhesion of cells to cells: a theoretical framework for adhesion mediated by  
366 reversible bonds between cell surface molecules. *Science* 200:618–627.
- 367 37. Bidone, T. C., A. V. Skeeters, P. W. Oakes, and G. A. Voth, 2019. Multiscale model of integrin adhesion assembly. *PLOS  
368 Computational Biology* 15:e1007077.
- 369 38. Takagi, J., K. Strokovich, T. A. Springer, and T. Walz, 2003. Structure of integrin  $\alpha 5\beta 1$  in complex with fibronectin. *The  
370 EMBO journal* 22:4607–4615.
- 371 39. Gaudet, C., W. A. Marganski, S. Kim, C. T. Brown, V. Gunderia, M. Dembo, and J. Y. Wong, 2003. Influence of type I  
372 collagen surface density on fibroblast spreading, motility, and contractility. *Biophysical journal* 85:3329–3335.
- 373 40. Neurohr, G. E., and A. Amon, 2020. Relevance and regulation of cell density. *Trends in cell biology* 30:213–225.
- 374 41. Brochu, T., and R. Bridson, 2009. Robust topological operations for dynamic explicit surfaces. *SIAM Journal on Scientific  
375 Computing* 31:2472–2493.

- 376 42. Li, F., S. D. Redick, H. P. Erickson, and V. T. Moy, 2003. Force measurements of the  $\alpha 5\beta 1$  integrin–fibronectin interaction.  
377 *Biophysical journal* 84:1252–1262.
- 378 43. Chen, W., J. Lou, J. Hsin, K. Schulten, S. C. Harvey, and C. Zhu, 2011. Molecular dynamics simulations of forced  
379 unbending of integrin  $\alpha V\beta 3$ . *PLoS computational biology* 7:e1001086.
- 380 44. García, A. J., J. E. Schwarzbauer, and D. Boettiger, 2002. Distinct activation states of  $\alpha 5\beta 1$  integrin show differential  
381 binding to RGD and synergy domains of fibronectin. *Biochemistry* 41:9063–9069.
- 382 45. Tan, S. J., A. C. Chang, S. M. Anderson, C. M. Miller, L. S. Prahl, D. J. Odde, and A. R. Dunn, 2020. Regulation and  
383 dynamics of force transmission at individual cell-matrix adhesion bonds. *Science Advances* 6:eaax0317.
- 384 46. Jahed, Z., H. Shams, M. Mehrbod, and M. R. Mofrad, 2014. Mechanotransduction pathways linking the extracellular  
385 matrix to the nucleus. *International review of cell and molecular biology* 310:171–220.
- 386 47. Shattil, S. J., C. Kim, and M. H. Ginsberg, 2010. The final steps of integrin activation: the end game. *Nature reviews  
387 Molecular cell biology* 11:288–300.
- 388 48. Takagi, J., B. M. Petre, T. Walz, and T. A. Springer, 2002. Global conformational rearrangements in integrin extracellular  
389 domains in outside-in and inside-out signaling. *Cell* 110:599–611.
- 390 49. Driscoll, T. P., T. C. Bidone, S. J. Ahn, A. Yu, A. Groisman, G. A. Voth, and M. A. Schwartz, 2021. Integrin-based  
391 mechanosensing through conformational deformation. *Biophysical journal* 120:4349–4359.
- 392 50. Mehrbod, M., S. Trisno, and M. R. Mofrad, 2013. On the activation of integrin  $\alpha IIb\beta 3$ : outside-in and inside-out pathways.  
393 *Biophysical journal* 105:1304–1315.
- 394 51. Su, S., Y. Ling, Y. Fang, and J. Wu, 2022. Force-enhanced biophysical connectivity of platelet  $\beta 3$  integrin signaling  
395 through Talin is predicted by steered molecular dynamics simulations. *Scientific reports* 12:4605.
- 396 52. Bidone, T. C., A. Polley, J. Jin, T. Driscoll, D. V. Iwamoto, D. A. Calderwood, M. A. Schwartz, and G. A. Voth, 2019.  
397 Coarse-grained simulation of full-length integrin activation. *Biophysical journal* 116:1000–1010.
- 398 53. Ji, Y., Y. Fang, and J. Wu, 2022. Tension Enhances the Binding Affinity of  $\beta 1$  Integrin by Clamping Talin Tightly: An  
399 Insight from Steered Molecular Dynamics Simulations. *Journal of Chemical Information and Modeling* 62:5688–5698.
- 400 54. Pan, D., and Y. Song, 2010. Role of altered sialylation of the I-like domain of  $\beta 1$  integrin in the binding of fibronectin to  
401  $\beta 1$  integrin: thermodynamics and conformational analyses. *Biophysical journal* 99:208–217.